Local Bandgap Variations In Moiré Structures - Origin And Parametric Dependence

A thesis
Submitted towards the partial fullfilment of
BS-MS dual degree programme
by

SHRIDHAR SANJAY SHANBHAG

Date: 15/03/2024

under the guidance of

Dr. Jan Wilhelm

Institute of Theoretical Physics
University of Regensburg

from May 2023 to Mar 2024

Indian Institute of Science Education and Research
Pune

Certificate

This is to certify that this dissertation entitled "Local Bandgap Variations In Moiré Structures - Origin And Parametric Dependence" submitted towards the partial fulfillment of the BS-MS degree at the Indian Institute of Science Education and Research, Pune represents original research carried out by Shridhar Sanjay Shanbhag at the University of Regensburg, under the supervision of Dr. Jan Wilhelm during academic year May 2023 to March 2024.

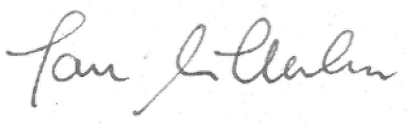

Supervisor:
Dr. Jan Wilhelm
Junior Group Leader
University of
Regensburg

Student:
Shridhar Sanjay Shanbhag
20191056
BS-MS
IISER Pune

Date:
15/03/2024

Declaration

I, hereby declare that the matter embodied in the report titled "Local Bandgap Variations In Moiré Structures - Origin And Parametric Dependence" is the result of the investigations carried out by me at the University of Regensburg from the period 15-05-2023 to 15-03-2024 under the supervision of Dr. Jan Wilhelm and the same has not been submitted elsewhere for any other degree.

Supervisor:
Dr. Jan Wilhelm
Junior Group Leader
University of
Regensburg

Student:
Shridhar Sanjay Shanbhag
20191056
BS-MS
IISER Pune

Date:
15/03/2024

Acknowledgements

I would like to express my heartfelt gratitude to my supervisor, Dr. Jan Wilhelm, for his support, guidance, and encouragement throughout the duration of my project. Dr. Wilhelm's expertise, patience, and mentorship have been invaluable to me, and I am deeply grateful for the opportunity to work under his supervision. His constructive feedback and insightful advice have played a crucial role in this project, and I am truly thankful for his dedication and commitment to my academic growth.

I would also like to extend my sincere gratitude to the University of Regensburg for providing me with the resources and environment conducive to my studies. The university has provided me with support and accomodation during my studies and has been very patient with my needs during my stay.

Additionally, I am grateful to my close friends and family for their love, encouragement, and understanding throughout this journey. Their constant support and encouragement have been a source of strength and motivation, without which life would have been very difficult and I am profoundly grateful for their presence in my life.

Contents

List of Figures

Abstract

A moiré pattern is a large scale interference pattern formed by the overlap of two small scale patterns with a small twist angle. A moiré structure can be formed by overlapping two 2D materials with similar structures and lattice constants over each other with a small twist angle. Moiré structures made from transition metal dichalcogenide bilayers show interesting properties such as a variation in the local band gap. This low-energy electronic structure can modeled as the properties of a single layer on which a periodic potential energy landscape is imposed. This periodic potential is called the moiré potential.

The extent to which the band edges vary in space is a measure of the moiré potential. Theoretical studies of the moiré potential based only on interlayer coupling without taking into account lattice relaxation effects calculate the size of this moiré potential to be of the order of tens of millielectronvolts [2]. Theoretical works that includes lattice relaxation effects calculate the moiré potential to be of the order of a hundred millielectronvolts [3], [4]. Experiments performed on the moiré structure formed by overlaying $MoSe_2$ on WSe_2 observed a moiré potential of the order of a hundred millielectronvolts [1]. The moiré potential of this magnitude is called a 'deep moiré potential' [1].

In this work, we implemented a method to study the moiré potential by using DFT to geometry optimize the structure and obtain the Local Density of States. We then use the LDOS to calculate the valence and conduction band edges and get an estimate of the moiré potential. We find that the extent of variation in the valence and conduction band edges thus obtained is of a similar order of magnitude as the ones obtained in experiments (deep moiré potentials). Furthermore, we use this method to understand the dependence of the moiré potential on the atomic reconstruction of the moiré cell.

Introduction

Atomically thin 2D materials have been extensively studied since the discovery of graphene in 2004 [5]. The study of isolated 2D systems led to studies of materials comprising of different layers of 2D materials stacked together called van der Waals heterostructures. These structures offer precise experimental control, allowing researchers to select the atomic species making up the semiconductors in each layer. Furthermore, by adjusting parameters like the relative twist angle between two layers, these structures can be used to create unique interference patterns called moiré patterns.

These moiré patterns create a superstructure with a moiré cell with atoms from both layers. This superstructure called the moiré structure has a periodicity that is much larger than that of the monolayer crystal lattice. Moiré patterns in 2D materials can be used to tune their electronic properties, which are fundamentally influenced by a periodic potential landscapes called the moiré potential. Moiré structures host a wide variety of interesting electronic phenomena such as the fractal quantum hall effect [6], tunable Mott insulators [7] and unconventional superconductivity [8]. Moiré structures can be made from a variety of 2D materials. In this thesis, we study the moiré structure made by two layers of transition metal dichalcogenide bilayers.

Transition metal dichalcogenides (TMDs) are 2D materials of the type MX_2 where M is a metal atom and X is a chalcogen atom. TMDs have interesting optical and electronic properties and became really popular after their band structure was systematically studied [9]. TMDs have weak dielectric screening and strong geometrical confinement that give rise to an extraordinarily strong coulomb interaction resulting in fascinating many body phenomena. One of these is the formation of strongly bound electron-hole pairs called excitons. Excitons are the fundamental electronic excitations in 2d semiconductors. They play a vital role in the optical response even at room temperature [10].

In TMD moiré structures, the electron-hole pair can exist either within a

layer or across layers. The moiré potential forms a potential energy landscape for these excitons impeding their free propagation. The excitons can get trapped in low energy pockets of the moiré potential [11].

Understanding the moiré potential is thus crucial to understanding many of the properties of moiré structures. Theoretical calculations based only on interlayer coupling estimate a very low value of the moiré potential ($\sim$ 10meV) [2]. The moiré potentials that are experimentally determined are over an order of magnitude larger and are called "deep" moiré potentials [1]. Theoretical work that includes lattice relaxation effects calculate the moiré potential to be of the order of a hundred millielectronvolts [3], [4].

The goal of this thesis is to use DFT to calculate the moiré potential for the moiré structure made from $MoSe_2$ on WSe_2 for small twist angles. We attempt to reproduce the results in the experimental paper [1] and analyse the dependence of the moiré potential on the system parameters such as the moiré wavelength, or the twist angle.

This thesis is structured as follows: Chapter 1 discusses the construction and mathematics of the moiré structures and briefly describes the TMD moiré cell and its regions of alignment. Chapter 2 introduces the theoretical foundations of DFT, and the methods used to compute the local density of states and the moiré potential. Chapter 3 and Chapter 4 present the results of our study and discusses them. Finally, the thesis concludes in Chapter 5, summarizing the key findings and proposing the direction for future research.

Chapter 1

Moiré Structures

Moiré patterns originate from the overlap of two or more periodic structures with a slight relative displacement or rotation or lattice constant mismatch. These patterns exhibit complex interference phenomena which have been studied in mathematics, physics and art. The term comes from a type of textile called 'moire' which is made by pressing two layers of silk cloth together when wet which creates a rippled effect due to the similar but imperfect spacing of the threads. Moiré structures or moiré materials are materials that arise when two similar 2D atomic lattices are stacked with a slight twist angle or misalignment with respect to each other.

In this chapter, we will provide the reader with a detailed understanding of moiré structures made from transition metal dichalcogenide (TMD) bilayers. TMD bilayers are a fascinating class of materials with unique electronic, optical and mechanical properties. In this thesis, we study the moiré structure made by overlaying Molybdenum Diselenide ($MoSe_2$) on Tungsten Diselenide (WSe_2) since detailed experimental analysis exists for this particular moiré structure provided in [1].

This chaptered is structured as follows: we shall describe the moiré patterns and the mathematical basis for understanding and constructing them in 1.1, we shall study the properties of transition metal dichalcogenides in 1.2 and the dynamics of excitons in TMD bilayers in 1.3.

1.1 Moiré Pattern

A moiré pattern is a large-scale interference pattern formed by overlaying two similar patterns with a slight difference, such as a shift, or a lattice constant

mismatch or a twist angle. A moiré pattern has a repeating structure and a super-cell made of both layers called the moiré cell. The length of this moiré cell is called the moiré wavelength or simply the moiré length.

The moiré length is a measure of spatial frequency of the lattice misalignment. It is analogous to beat frequency in audio waves with different wavelengths. The superposition of two waves with wave vectors $\vec{k_1}$ and $\vec{k_2}$ is given by,

$$A(\vec{r}) = \sin\left(\vec{k_1} \cdot \vec{x}\right) + \sin\left(\vec{k_2} \cdot \vec{x}\right) = \sin\left(\frac{\vec{k_1} + \vec{k_2}}{2} \cdot \vec{x}\right) \cos\left(\frac{\vec{k_1} - \vec{k_2}}{2} \cdot \vec{x}\right)$$

Consider $\vec{k_1}$ and $\vec{k_2}$ to be waves along one of the principal axes of the unit cells of the two structures with a wavelength equal to the cell length. For similar wave vectors, the function has a small wavelength pattern due to the sum of the wave vectors in the sine term and a long wavelength pattern due to the difference of the wave vectors in the cosine term. The moiré wavelength is the result of the long wavelength pattern since the small wavelength pattern is smaller than atomic legth scales. Therefore,

$$\lambda_{\text{moiré}} \approx \frac{4\pi}{\left|\vec{k_1} - \vec{k_2}\right|}$$

Generally, the larger the twist angle, the larger is the difference between $\vec{k_1}$ and $\vec{k_2}$, and the smaller the moiré length as shown in figure 1.1.

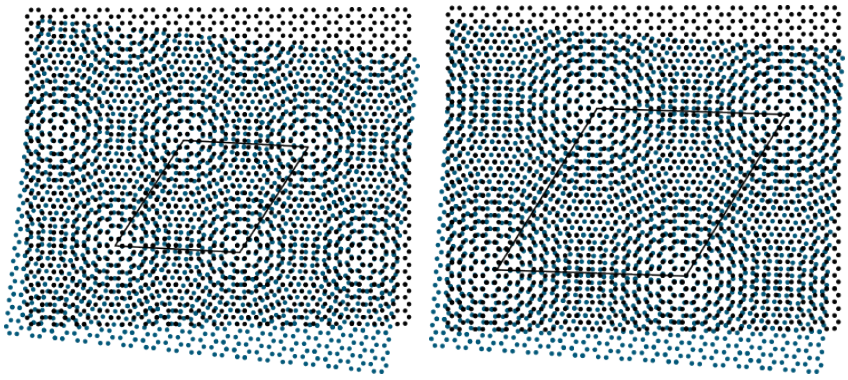

(a) Twist angle: 6° (b) Twist angle: 4°

Figure 1.1: Moiré patterns made from the overlap of two identical hexagonal lattices

As shown in figure 1.1, the moiré cell has regions within it with different types of lattice misalignment. Understanding these regions is crucial for our

understanding of moiré structures in condensed matter physics as we shall see in the following sections.

1.2 Transition Metal Dichalcogenide Bilayers

In this thesis, we study the properties of moire structures formed by layering transition metal dichalcogenide (TMD) bilayers. TMDs are 2D semiconductors of the type MX_2, where M is a transition metal atom (such as Mo, W, etc.), and X is a chalcogen atom (such as Se, S or Te). Structurally, these semiconductors are of the 2H form which is a hexagonal phase with a honeycomb lattice, similar to graphene. Each unit cell has one metal atom in-plane and two nonmetal atoms above and below the plane as shown below. Thus, they have a lattice structure of a honeycomb where each lattice point is alternatively a metal atom or a dichalcogen pair. This leads to a broken inversion symmetry which is not present in materials like graphene.

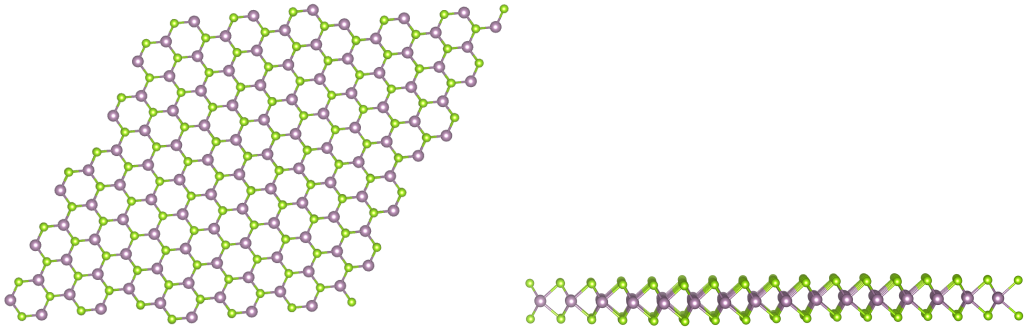

(a) Structure seen from above (b) Structure seen from the side

Figure 1.2: Structure of a hexagonal TMD monolayer

TMD bilayers are of two kinds - homobilayers, where the two layers are chemically identical and heterobilayers, where the two layers are chemically distinct. In this thesis, we study the TMD heterobilayer formed by $MoSe_2$ on WSe_2.

The broken inversion symmetry in TMDs results in two distinct aligned stacking configurations termed R (0° alignment between the two layers) and H (180° alignment between the two layers) as shown below [1]. Three types of stacking orders exist for R-stacked bilayers. These are called R^M_M(same as R^X_X), R^M_X and R^X_M [1]. Here, R^M_X refers to a kind of R-stacking where the metal atom of the upper layer is directly above a nonmetal atom of the lower

layer [1]. Similarly, the three types of stacking orders for H-stacked bilayers are H^M_M, H^M_X(same as H^X_M) and H^X_X [1].

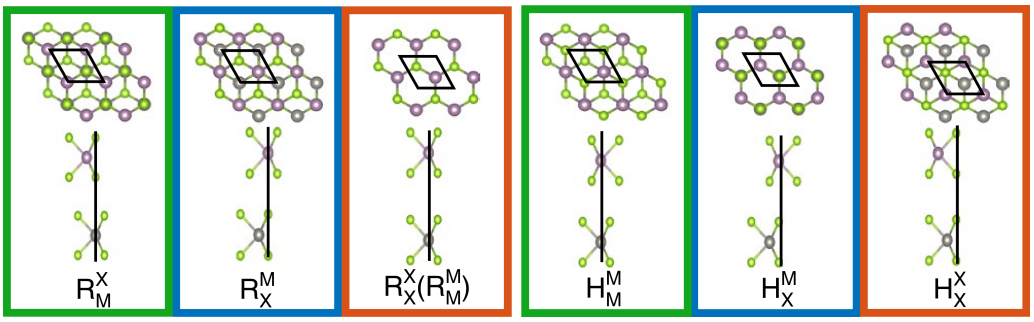

(a) R-stacked (b) H-stacked

Figure 1.3: **High-symmetry stacking configurations in heterobilayers** (taken from [1])

All three stacking orders are in every moire cell for a nearly H-stacked twisted bilayer as seen in figure 1.4.

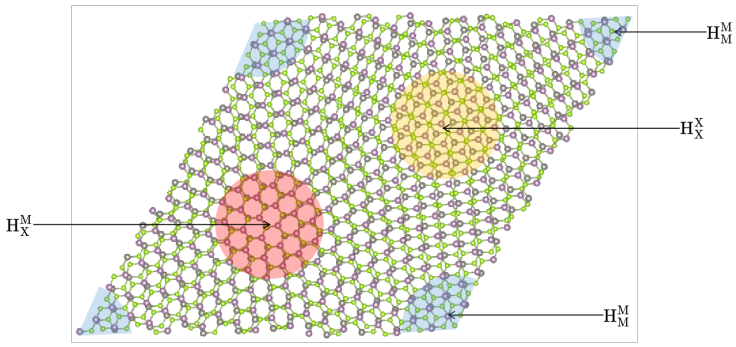

Figure 1.4: **A TMD moiré cell** consisting of 2010 atoms made by overlaying $MoSe_2$ on WSe_2. The red region has H^M_X (same as H^X_M), the yellow region has H^X_X and the blue region in the corners has H^M_M

The difference in the local interlayer alignment of the atoms leads to different local bandgaps in each region. The moiré structure in effect has repeating local regions with different band edges and different interlayer gaps.

The low energy band variations can be modeled as the result of a spatially periodic potential energy landscape being imposed on a sinlge layer. This potential energy landscape is termed as the moiré potential. As a result

of the moiré potential, many interesting emergent quantum phenomena have been observed in twisted TMD bilayers. One of the exciting fields of research is the study of exciton dynamics in these materials.

1.3 Exciton Dynamics in Moiré Patterns

In 2D semiconductors, excitons are the fundamental electronic excitations. They are bound states of an electron and a hole attracted to each other by the Coulomb force. In the context of two-dimensional transition metal dichalcogenide (2D TMD) structures, excitons are of particular interest due to the unique characteristics of these materials.

The 2D nature of TMD structures, coupled with weak dielectric screening, leads to very strong coulomb interactions, resulting in the formation of strongly bound electron-hole pairs upon optical excitation [10]. This enhanced interaction significantly influences the behavior and properties of excitons in these systems, making them intriguing subjects for study [12].

Moiré excitons represent a specialized category of excitons within TMD structures. They refer to photo-excited electron-hole bound states that form within a layer or across two layers and are termed as intralayer and interlayer excitons respectively. These excitons are influenced by the moiré potential which creates a distinct potential energy landscape for them.

The presence of various regions with different local interlayer alignment in TMD moiré structures can greatly alter the electronic band structure of the material. This alteration manifests as the formation of miniband structures and flat bands, directly impacting the material's transport behavior and electronic properties [12].

As a consequence of these unique electronic structures, moiré excitons give rise to several interesting quantum phenomena and many-body effects, including exciton condensation, superfluidity, and the emergence of topologically protected states [12]. Understanding these phenomena is essential for harnessing the full potential of TMD moiré structures in future technological applications.

One significant aspect of moiré excitons is their confinement within low-energy pockets of the moiré potential, which impedes their free propagation

within the material [10]. This confinement has implications for the material's optical and electronic response, making it crucial to study and understand the underlying causes and parameters governing the moiré potential [10].

The two-dimensional nature of TMD structures facilitates experimental investigation using techniques such as scanning tunneling microscopy (STM) [10], providing valuable insights into the behavior and properties of excitons that are not easily accessible in the study of bulk 3D materials.

Thus, understanding moiré potentials is very important to understanding the electronic properties and the behaviour of excitons in TMD moiré structures. In this thesis, we use DFT calculations on the entire moiré cell (as is done in [13]) to accurately determine the band edges and understand the moiré potential.

Chapter 2

Density Functional Theory

Density Functional Theory (DFT) is a powerful tool in modern computational condensed matter physics used to study the electronic and nuclear structure of molecules and condensed matter materials. It was developed by Walter Kohn, Pierre Hohenberg and Lu Jeu Sham in 1964-65 [14] [15]. DFT is based on the idea that any characteristic of a system made of interacting particles can be written as a function of the ground state density $n(\mathbf{r})$. This scalar function depends only on the position but, in principle, contains all the information required to construct the many-body wave function. This chapter aims to provide the reader with the theoretical foundations of density functional theory, followed by a discussion of Kohn-Sham DFT. We describe the self consistent field method for solving the underlying equations numerically using gaussian basis sets. We then describe the local density of states and how we compute it from the Kohn-Sham states. Finally, the chapter concludes with a description of the valence band and conducting band and how we calculate it for our system. The main reference for this chapter is the book by Robert G. Parr and Yang Weitao [16].

2.1 The Many Body Problem

For any time-independent, non-relativistic quantum mechanical system, the Schrödinger equation [16] is given by

$$\hat{H} \left|\Psi_n\right\rangle = E_n \left|\Psi_n\right\rangle \tag{2.1}$$

Here, $\hat{H}$ is the Hamiltonian of the system and $|\Psi_n\rangle$ is the nth eigenstate of the system with corresponding energy E_n. The Hamiltonian consists of five parts for a system of interacting nuclei and electrons.

$$\widehat{H} = \widehat{T}_{nucl} + \widehat{T}_e + \widehat{V}_{nucl,\,nucl} + \widehat{V}_{nucl,\,e} + \widehat{V}_{e,\,e} \tag{2.2}$$

The first two terms are the kinetic energy of the nuclei and the electrons, respectively.

$$\widehat{T}_{nucl} = -\sum_{A} \frac{\hbar^2}{2M_A} \boldsymbol{\nabla}^2_{R_A} \tag{2.3}$$

$$\widehat{T}_{e} = -\frac{\hbar^2}{2m} \sum_{i} \boldsymbol{\nabla}^2_{r_i} \tag{2.4}$$

Here, the mass of the electron is represented by m, and their coordinates are represented by r_i. R_A, represent the atomic coordinates and M_A represents their masses. The other three terms are the potential energies due to the coulomb interaction between the particles.

$$\widehat{V}_{nucl,\, nucl} = \sum_{A} \sum_{B>A} \frac{Z_A Z_B e^2}{|R_A - R_B|} \tag{2.5}$$

$$\widehat{V}_{e,\, e} = \sum_{i} \sum_{j>i} \frac{e^2}{|r_i - r_j|} \tag{2.6}$$

$$\widehat{V}_{nucl,\, e} = -\sum_{A} \sum_{i} \frac{Z_A e^2}{|r_i - R_A|} \tag{2.7}$$

The Schrödinger equation then becomes,

$$\hat{H}(\underline{\mathbf{r}}, \underline{\mathbf{R}}) \Psi(\underline{\mathbf{r}}, \underline{\mathbf{R}}) = E \Psi(\underline{\mathbf{r}}, \underline{\mathbf{R}})$$

where, $\underline{\mathbf{r}}$ is the ordered set of all electron coordinates and $\underline{\mathbf{R}}$ is the ordered set of all atomic nuclei coordinates.

The above Hamiltonian ignores relativistic effects and magnetic interactions, including orbit-orbit, spin-orbit and spin-spin interactions. This Hamiltonian also treats both electrons and nuclei on the same footing as quantum mechanical objects. However, electrons are very light and cannot be described by classical mechanics, while nuclei, being thousands of times heavier display only small quantum effects in comparison. This large mass difference leads to nuclei having significantly smaller velocities than electrons. Thus, electrons adjust to a change in the nuclear geometry very quickly.

We thus use the Born-Oppenheimer approximation which decouples the wavefunction of the nuclei (Ψ_{nucl}) and the wavefunction of the electrons (Ψ_e),

$$\Psi(\underline{\mathbf{r}}, \underline{\mathbf{R}}) = \Psi_{nucl}(\underline{\mathbf{R}}) \Psi_e(\underline{\mathbf{r}}) \tag{2.8}$$

According to this approximation, the electron wavefunction obeys the Schrödinger equation,

$$\hat{H}_{e,\underline{\mathbf{R}}}(\underline{\mathbf{r}})\Psi_{e,\underline{\mathbf{R}}}(\underline{\mathbf{r}}) = E_e\Psi_{e,\underline{\mathbf{R}}}(\underline{\mathbf{r}}) \tag{2.9}$$

with

$$\hat{H}_{e,\underline{\mathbf{R}}} = \hat{T}_e(\underline{\mathbf{r}}) + \hat{V}_{nucl\ e,\underline{\mathbf{R}}}(\underline{\mathbf{r}}) + \hat{V}_{ee}(\underline{\mathbf{r}}) + V_{nucl\ nucl,\underline{\mathbf{R}}} \tag{2.10}$$

Here, $\underline{\mathbf{R}}$ are only parameters of the nuclei position and thus, $V_{NN,\underline{\mathbf{R}}}$ is just a number. The above Hamiltonian can be used to solve the Schrödinger equation to find the many-body wavefunction analytically. In principle, we are done. The many-body wavefunction yields all the physical properties of the system. However, an analytical solution for the many-body system is difficult to obtain for any system with more than one electron, so we rely on numerical methods.

A standard way to solve a partial differential equation is to discretize the space into a grid. Let us assume that N_{grid} grid points are used to discretize the space. The Schrödinger equation then becomes an eigenvalue equation where $|\Psi_n\rangle$ has N_{grid}^N entries, and the Hamiltonian has $N_{grid}^N \times N_{grid}^N$ entries. Solving the eigenvalue problem thus requires $N_{op} = N_{grid}^{3N}$ floating point operations on a computer. The computing time thus grows exponentially with the number of electrons. With even 100 grid points in any direction, it would take the largest supercomputers in the world longer than the age of the universe to compute the solution to the many-body Schrödinger equation for a moiré cell.

This makes it computationally infeasible to solve the Schrödinger equation for moiré structures, motivating the use of a different approach.

2.2 The Electron Density

In this thesis, we use Density Functional Theory (DFT) to calculate the properties of the moiré structures. In DFT, we optimize the electron density $n(\mathbf{r})$ to minimize the ground state energy E in the Schrödinger equation. Numerically, this method has the advantage that we have only a single variable $n(\mathbf{r})$ instead of a large number of variables in the wavefunction.

2.2.1 Definition of the electron density

The electron density operator $\hat{n}$ is defined as

$$\hat{n}(\mathbf{r}) = \sum_{i=1}^{N} \delta(\mathbf{r} - \mathbf{r}_i) \tag{2.11}$$

where $\mathbf{r}_i$ is the coordinate of electron i and N is the total number of electrons in our system. The electron density $n(\mathbf{r})$ of a system in a state with an electronic wavefunction Ψ is defined as the expectation value of the electron density operator,

$$\begin{aligned} n(\mathbf{r}) &= \langle \Psi | \, \hat{n}(\mathbf{r}) \, | \Psi \rangle \\ &= \int d\mathbf{r}_1 d\mathbf{r}_2 \ldots d\mathbf{r}_N \Psi^*(\mathbf{r}_1, \mathbf{r}_2, \ldots, \mathbf{r}_N) \hat{n}(\mathbf{r}) \Psi(\mathbf{r}_1, \mathbf{r}_2, \ldots, \mathbf{r}_N) \\ &= N \int d\mathbf{r}_2 d\mathbf{r}_3 \ldots d\mathbf{r}_N |\Psi(\mathbf{r}_1, \mathbf{r}_2, \ldots, \mathbf{r}_N)|^2 \end{aligned}$$

where Ψ is the many-electron wavefunction of the system.

2.2.2 Properties of the electron density

The electron density has the following notable properties:

1. The electron density $n(\mathbf{r})$ is normalized to the number of electrons,

$$\int n(\mathbf{r}) d^3\mathbf{r} = N \tag{2.12}$$

2. It is non-negative everywhere,

$$n(\mathbf{r}) \geq 0 \tag{2.13}$$

3. If $\Psi_{SD}(\mathbf{r}_1, \mathbf{r}_2, \ldots, \mathbf{r}_N)$ is a Slater determinant with $\psi_i(\mathbf{r})$ as the single particle orbitals, the electron density is given by,

$$n(\mathbf{r}) = \sum_{i=1}^{N} |\psi_i(\mathbf{r})|^2 \tag{2.14}$$

2.3 Hohenberg-Kohn Theorems

The Hohenberg-Kohn theorems (HKTs) introduced by Pierre Hohenberg and Walter Kohn form the main principles of DFT [14].

The HKTs assume that the many-electron Hamiltonian is of the form:

$$\hat{H} = \hat{T}(\underline{\mathbf{r}}) + \hat{V}_{ext}(\underline{\mathbf{r}}) + \hat{V}_{ee}(\underline{\mathbf{r}}) \tag{2.15}$$

where,

$$\hat{V}_{ext}(\underline{\mathbf{r}}) = \int d^3\mathbf{r}\; v_{ext}\hat{n}(\mathbf{r}) = \sum_{i=1}^{N} v_{ext}(\mathbf{r}_i) \tag{2.16}$$

In the case of an external potential caused by the Coulombic attraction between the electrons and the nuclei,

$$v_{ext}(\mathbf{r}) = -\sum_{A} \frac{Z_A e^2}{|\mathbf{r} - \mathbf{R}_A|} \tag{2.17}$$

A pre-requisite to understanding the Hohenberg-Kohn theorems is the concept of function space and functionals. We define the function space L_N as

$$L_N = \left\{ \tilde{n} : \mathbb{R}^3 \to \mathbb{R} \text{ with } \int \tilde{n}(\mathbf{r})\; d^3\mathbf{r} = N \text{ and } \tilde{n}(\mathbf{r}) \geq 0 \;\forall\; \mathbf{r} \in \mathbb{R}^3 \right\} \tag{2.18}$$

this means that L_N contains all possible electron densities with N electrons. A functional $F : L_N \to R$ is a map that maps a function (in our case, an electron density) to a single real number.

The Hohenberg-Kohn theorems are as follows:

1. The ground state electron density $n_0(\mathbf{r})$ uniquely determines the external potential $v_{ext}(\mathbf{r})$ up to an additive constant.

2. There exists a total energy functional $E[\tilde{n}]$ of the form

$$E[\tilde{n}] = F[\tilde{n}] + \int d^3\mathbf{r}\; v_{ext}(\mathbf{r})\; \tilde{n}(\mathbf{r}) \tag{2.19}$$

   such that the ground state energy E of a many-electron system in an external potential $v_{ext}(\mathbf{r})$ is obtained when minimizing $E[\tilde{n}]$ among all electron densities $\tilde{n}(\mathbf{r}) \in L_N$:

$$E = \min_{\tilde{n} \in L_N} E[\tilde{n}] \tag{2.20}$$

   The functional $F[\tilde{n}]$ is a universal functional independent of v_{ext}.

The first HKT implies a one-to-one mapping between the ground state density and the external potential. The second HKT states that we can find the ground state energy E and the ground state density $n(\mathbf{r})$ of a many-electron system with external potential v_{ext} (e.g. given by the atomic nuclei) by minimizing the total energy functional $E[\tilde{n}]$ by varying $\tilde{n}(\mathbf{r})$. The exact form of the functional $F[\tilde{n}]$ is unknown, and approximate forms are used to enable DFT calculations in practice. The functional $F[n]$ comprises all energy (kinetic energy and electron-electron interaction) of the many-electron state except for the interaction with the external potential. The kinetic energy and the electron-electron interaction are difficult to compute accurately solely from the electron density. This problem can be avoided using Kohn-Sham DFT, as described in the following section.

2.4 Kohn-Sham DFT

Kohn-Sham DFT is a method introduced by Walter Kohn and Lu Sham [15] in which we avoid the problem of inaccurate kinetic energy and our inability to compute the electron-electron interaction by expressing the electron density using Kohn-Sham orbitals.

2.4.1 Kohn-Sham orbitals

In this thesis, we assume that all Kohn-Sham orbitals are doubly filled, and thus the electron density is given by

$$n(\mathbf{r}) = 2\sum_{i=1}^{N} |\psi_i(\mathbf{r})|^2 \tag{2.21}$$

where $\psi_i(\mathbf{r})$ are the Kohn Sham orbitals that are under the constraint of orthonormality,

$$\langle \psi_i | \psi_j \rangle = \int d^3\mathbf{r} \psi_i^*(\mathbf{r}) \psi_j(\mathbf{r}) = \delta_{ij}$$

2.4.2 Approximation to kinetic energy

Introducing orbitals allows us to approximate the kinetic energy as

$$T_s[\psi_1, \psi_2, \ldots, \psi_N] := \sum_{i=1}^{N} -\frac{\hbar^2}{2m} \langle \psi_i | \boldsymbol{\nabla}^2 | \psi_i \rangle \tag{2.22}$$

The total energy functional $E[n]$ is:

$$E[n] = T[n] + E_H[n] + E_{xc}[n] + E_{ext}[n] \tag{2.23}$$

Where, the Hartree energy $E_H[n]$ given by

$$E_H[n] = \frac{1}{2} \int \int d^3\mathbf{r} d^3\mathbf{r}' \, \frac{n(\mathbf{r})n(\mathbf{r}')}{|\mathbf{r} - \mathbf{r}'|} \tag{2.24}$$

$E_{ext}[n]$ is the external potential energy,

$$E_{ext}[n] := \int d\mathbf{r}^3 \, v_{ext}(\mathbf{r}) \, n(\mathbf{r}) \tag{2.25}$$

$E_{xc}[n]$ is the exchange-correlation energy that contains all electron-electron interactions beyond the Hartree energy.
Since the kinetic energy functional described above is valid only for the non-interacting system, to account for the interaction effects, the exchange-correlation functional in KS-DFT includes the difference between the true kinetic energy functional $T[n]$ and the single-particle kinetic energy functional $T_s[n]$

$$E_{xc}^{KS} := E_{xc} + T[n] - T_s[n] \tag{2.26}$$

The total energy functional then becomes,

$$\begin{aligned} E[n] &= T[n] + E_H[n] + E_{xc}[n] + E_{ext}[n] \\ &= T_s[n] + E_H[n] + (E_{xc}[n] + T[n] - T_s[n]) + E_{ext}[n] \\ &= T_s[n] + E_H[n] + E_{xc}^{KS} + E_{ext}[n] \end{aligned}$$

Thus, the total energy E can be computed from the minimization

$$E = \min_{n(\mathbf{r})} E[n] = \min_{n(\mathbf{r})} \left[T_s[n] + E_H[n] + E_{xc}^{KS}[n] + E_{ext}[n] \right] \tag{2.27}$$

2.4.3 Kohn-Sham equations

The minimization procedure of the total energy is done by setting up a Lagrangian constrained by the orthonormal condition of the KS-orbitals. Solving the minimization problem leads to the Kohn-Sham equations [15]:

$$\left[-\frac{\hbar^2}{2m} \boldsymbol{\nabla}^2 + v_{ext}(\mathbf{r}) + v_H(\mathbf{r}) + v_{xc}(\mathbf{r}) \right] \psi_i(\mathbf{r}) = \epsilon_i \psi_i(\mathbf{r}) \tag{2.28}$$

The KS-eigenvalues ϵ_i result from the Lagrangian optimization procedure and, therefore, cannot be interpreted as the eigenvalues of the Schrödinger equation. The KS equation contains the external potential $v_{ext}(\mathbf{r})$, the Hartree potential $v_H(\mathbf{r})$, the exchange-correlation potential $v_{xc}(\mathbf{r})$ and the kinetic energy term. The derivative of the exchange-correlation energy functional with respect to the electron density gives the exchange-correlation potential.

$$v_{xc}(\mathbf{r}) = \frac{\delta E_{xc}[n]}{\delta n(\mathbf{r})} \tag{2.29}$$

The Hartree potential is the Coulomb interaction between the electron and the electron density given by the KS-orbitals

$$v_H(\mathbf{r}) = e^2 \int d^3\mathbf{r}' \frac{\sum_{i=1}^{N} |\psi_i(\mathbf{r}')|^2}{|\mathbf{r} - \mathbf{r}'|} \tag{2.30}$$

If the true form of $E_{xc}[n]$ was known, the system's exact ground-state energy and density could be found. However, no exact closed form for $E_{xc}[n]$ is known, and current implementations of KS-DFT rely on approximate exchange-correlation functionals. Since the Hartree and exchange-correlation potential depend on the KS-Orbital, the equation must be solved self-consistently, as described in the following section.

2.5 Self-consistent Field Cycle

The Kohn-Sham equations are a set of equations that depend on the potentials shown in equations (2.30), (2.29), and (2.17) [17]. Since this effective potential depends on the electron density, the calculation of this density is done via an iterative scheme called the self-consistent field cycle as described below [17].

1. The SCF cycle starts with an inital guess of the electron density, n_{in}. In our study, we use the superposition of atomic densities.

2. The next step in the process is to calculate the potentials $v_H(\mathbf{r})$, and $v_{xc}(\mathbf{r})$ from the density as shown in equations (2.30), and (2.29).

3. These are then used as input in the Kohn-Sham equation to obtain the eigenvalues (ϵ_i) and the eigenvectors (ψ_i).

$$\left[-\frac{\hbar^2}{2m}\boldsymbol{\nabla}^2 + v_{ext}(\mathbf{r}) + v_H(\mathbf{r}) + v_{xc}(\mathbf{r})\right]\psi_i(\mathbf{r}) = \epsilon_i\psi_i(\mathbf{r})$$

   This is the most computationally expensive part of the SCF cycle.

4. The eigenfunctions ψ_i are used to compute the density.

$$n(r) = 2\sum_{i=1}^{N} |\psi_i(\mathbf{r})|^2$$

This new density differs from the initial density and the process is restarted with this new density to calculate the potentials as in step 2.

5. The difference between the input and output density is decreasing with each iteration. The SCF cycle is stopped once the difference between the densities is below a specified threshold.

6. Once the density has converged, the total energy E_{KS} is calculated giving us the required estimate of the ground state energy of the system.

$$E_{KS}[n] = T_s[n] + E_H[n] + E_{xc}^{KS}[n] + \int d\mathbf{r} v_{ext}(\mathbf{r}) n(\mathbf{r}) \tag{2.31}$$

An accurate estimation of the ground state energy and density requires a good choice of exchange correlation functional and a basis set in which to represent the KS-orbitals as we shall see in the following sections.

2.6 Exchange-Correlation Functional

A crucial part of determining the accurate ground state density is the choice of the exchange-correlation functional which is responsible for capturing the electron-electron interaction effects that are beyond the Hartree potential. Since no closed form of E_{xc}^{ks} exists, many approximate functionals have been developed with various levels of accuracy [18]. The most simple exchange correlation functional is the Local Density Approximation(LDA). LDA assumes a homogeneous electron gas in a volume $d^3\mathbf{r}$ and the exchange-correlation functional is approximated to have the form

$$E_{xc}^{LDA}[n] = \int d^3\mathbf{r}\ n(\mathbf{r}) \epsilon_{xc}(n(\mathbf{r})) \tag{2.32}$$

where ϵ_{xc} is the exchange correlation energy per electron of a homogeneous electron gas.
A more sophisticated approach is to include information on the gradient of the density which introduces non-local effects. Exchange-correlation functionals that include the gradient $\boldsymbol{\nabla} n(\mathbf{r})$ are categorized as Generalized Gradient Approximation (GGA) functionals.

The general form of GGA functionals is

$$E_{xc}^{GGA}[n] = \int d^3\mathbf{r}\; n(\mathbf{r})\; f(n(\mathbf{r}), \boldsymbol{\nabla} n(\mathbf{r})) \tag{2.33}$$

The most commonly used GGA functional is the Perdew-Burke-Ernzerhof (PBE) functional. It is applicable to a wide range of systems and it does not depend on experimentally fitted parameters. The PBE functional has parameters that have been determined to satisfy exact conditions for a few systems where the exact functional form is known. In this thesis, the PBE functional is used for all DFT calculations.

2.7 Basis Sets

To solve the KS-equation numerically, we use basis sets to represent the KS-orbitals. Each KS-orbital is represented as a linear combination of known basis functions $\phi_\nu(\mathbf{r})$,

$$\psi_n^{KS}(r) = \sum_{\nu=1}^{N_b} C_{n\nu}\phi_\nu(r)$$

where, $C_{n\nu}$ are the corresponding expansion coefficients.
An exact representation of the KS orbitals in a given basis would require an infinite coordinate system spannned by the complete basis set with $N_b \to \infty$ [18]. However, this is not feasible since the computational cost of solving the KS-equation scales with $\mathcal{O}(N_b^3)$. There are various types of basis functions $\phi_\nu(r)$ that can be used to expand the KS-orbitals such as the plane wave basis set, Gaussian-type orbitals etc. [18].

In this thesis, we use the Gaussian orbitals for all DFT calculations. These have the general form,

$$\phi_\nu(r) = Y_{l,m}(\theta, \varphi) r^{2n-2-l} e^{-\zeta r^2}$$

where, $Y_{l,m}(\theta, \varphi)$ are the spherical harmonics. The index l,n and m determine the type of orbital and ζ defines the width of the Gaussian funtion.

Basis sets are classified based on the number of functions used. The smallest basis set is the *minimum basis set*, which has only enough functions to account for all electrons of the neutral atom. The next larger basis set is called Double Zeta Valence Polarization (DZVP). DZVP contains twice as

many basis functions for each orbital as indicated by the D. The zeta refers to the exponent in the gaussian function [17]. As the inner orbitals change less when a chemical bond is formed, the basis set only uses two sets of basis functions for the Valence orbitals as indicated by the V in the name. P stands for polarization, which refers to the use of additional basis functions to introduce more flexibility. This is due to the fact that when electrons interact with each other, the resulting charge distribution will be distorted which can be addressed by introducing polarization functions, which are higher angular momentum functions.

2.8 Geometry Optimization

In this thesis, we study moiré structures which have supercells with different regions of alignment as discussed in the previous chapter. Due to the various angles and strain values of the structures studied, it is not possible for us to use experimental values for the position of the atoms because, for many of the structures studied, it is likely that no experimental data on atomic positions exists. In order to calculate the physical properties of the moiré structures, we need the positions of every atomic nucleus. One way to get the positions of atomic nuclei is to use the geometry that has the lowest total energy among all geometries of the system. Geometry optimization is the process of changing the system's geometry by varying the nuclear coordinates to minimize the total energy of the system [18].

2.8.1 Potential energy surface

Consider a system with K atomic nuclei. Let $\underline{\mathbf{R}} = (\mathbf{R}_1, \mathbf{R}_2, \ldots, \mathbf{R}_K)$ be the positions of the nuclei. The ground state energy $E_{\underline{R}}$ of the electronic system is then parametrized by the nuclear positions.
We can consider $E(\underline{\mathbf{R}})$ as a function of the atomic positions that depends on $3K$ variables (3 spatial coordinates for each of the K atoms). This function is called the potential energy surface. The reason for this name is that we have a $3K$-dimensional plane above which there is a continuous potential energy surface with height $E(\underline{\mathbf{R}})$.

2.8.2 Algorithms for Geometry Optimization

Geometry optimization relies on numerical minimization schemes to find a local minimum of the potential energy surface [16]. One simple method is called gradient descent minimization.

The gradient descent method repeatedly takes a step in direction of the negative gradient of f:

$$\mathbf{x}_{n+1} = \mathbf{x}_n - k_n \boldsymbol{\nabla} f(\mathbf{x}_n)$$

where k_n is the step size that is adjusted in the n^{th} iteration using the line search procedure,

$$k_n = \arg\min_k [f(\mathbf{x}_n - k\boldsymbol{\nabla} f(\mathbf{x}_n))]$$

Another popular method is the Broyden–Fletcher–Goldfarb–Shanno (BFGS) algorithm as described below:
With an initial guess $\underline{\mathbf{R}_0}$, and an initial guess of the Hessian matrix B_0, the following steps are repeated:

1. Obtain a direction $\underline{\mathbf{p}_k}$ by solving

$$B_n \underline{\mathbf{p}_n} = -\boldsymbol{\nabla} E(\underline{\mathbf{R}_n})$$

2. Using the line search procedure, find an acceptable step size k_n

$$k_n = \arg\min_k [E(\underline{\mathbf{R}_n} + k\underline{\mathbf{p}_n})]$$

3. Let $\underline{\mathbf{s}_n} = k\underline{\mathbf{p}_n}$ and update $\underline{\mathbf{R}_{n+1}} = \underline{\mathbf{R}_n} + k\underline{\mathbf{p}_n}$
4. $\underline{\mathbf{y}_k} = \boldsymbol{\nabla} E(\underline{\mathbf{R}_{n+1}}) - \boldsymbol{\nabla} E(\underline{\mathbf{R}_n})$
5. $B_{k+1} = B_k + \frac{\mathbf{y}_k \mathbf{y}_k^T}{\mathbf{y}_k^T \mathbf{s}_k} - \frac{B_k \mathbf{s}_k \mathbf{s}_k^T B_k^T}{\mathbf{s}_k^T B_k \mathbf{s}_k}$

The above steps are repeated until $\underline{\mathbf{R}_n}$ converges to the solution.

2.8.3 Force Calculation

As seen above, the gradient $\boldsymbol{\nabla} E(\underline{\mathbf{R}})$ needs to be computed for geometry optimization. A theorem that is useful in the calculation of these energy gradients is the Feynman-Hellman theorem [19] [20].
If λ is any parameter of the system, and $\hat{H}_\lambda$ is the parametrized Hamiltonian, and the Schrödinger equation is given by,

$$\hat{H}_\lambda \Psi_\lambda = E_\lambda \Psi_\lambda, \tag{2.34}$$

then, the derivative of the eigenvalue $E_\lambda = \langle \Psi_\lambda | \hat{H}_\lambda | \Psi_\lambda \rangle$ is given by

$$\frac{\partial E_\lambda}{\partial \lambda} = \left\langle \Psi_\lambda \left| \frac{\partial \hat{H}_\lambda}{\partial \lambda} \right| \Psi_\lambda \right\rangle \tag{2.35}$$

and so, no derivatives on Ψ_λ need to be evaluated.
The proof of the Hellmann-Feynman theorem relies on the assumption that we use an infinite basis set for our calculations. As a consequence, when comparing numerically computed forces with the Hellmann-Feynman force for special cases, large discrepancies are observed. The reason is that we always use a finite basis set to compute the wavefunction Ψ.
Consequently,

$$\begin{aligned}\frac{\partial E(\underline{\mathbf{R}})}{\partial \underline{\mathbf{R}}} &= \left\langle \frac{\partial \Psi}{\partial \underline{\mathbf{R}}} \left| \hat{H} \right| \Psi_\lambda \right\rangle + \left\langle \Psi_\lambda \left| \hat{H} \right| \frac{\partial \Psi}{\partial \underline{\mathbf{R}}} \right\rangle + \left\langle \Psi_\lambda \left| \frac{\partial \hat{H}}{\partial \underline{\mathbf{R}}} \right| \Psi_\lambda \right\rangle \\ &\neq \left\langle \Psi_\lambda \left| \frac{\partial \hat{H}}{\partial \underline{\mathbf{R}}} \right| \Psi_\lambda \right\rangle\end{aligned}$$

So, we need to take the derivative of the wavefunction, $\partial\Psi/\partial\underline{\mathbf{R}}$ explicitly into account while using a finite basis. The additional derivatives of the wavefunction contribute to Pulay forces which are defined as the additional force to the Hellmann-Feynman force due to the derivative of the wavefunction. In most DFT implementations the pulay forces are also computed along with the Hellman-Feynman forces.

The next section gives a description of the local density of states and provides a numerical way to compute it from DFT.

2.9 Local Density Of States

For any physical system, the density of states (DOS) is defined as the number of available electronic states within a volume V per unit energy interval per unit volume [16]. The density of states is thus defined as,

$$\rho(E) = \frac{N(E)}{V} \tag{2.36}$$

where $N(E)\delta E$ is the number of states in the system of volume V whose energies lie in the range E to $E + \delta E$. In general, the density of states of a system of volume V and N countable energy levels is defined as:

$$\rho(E) = \frac{1}{V}\sum_{i=1}^{N} \delta(E - \epsilon_i) \tag{2.37}$$

where, ϵ_i is the energy of the i^{th} state.
The local density of states(LDOS) is a space resolved density of states. LDOS (denoted as $\rho(\vec{r}, E)$) is thus a measure of number of electronic states available per unit energy per unit volume at a specific point in space.
For a system of non-interacting electrons,

$$\rho(\vec{r}, E) = \sum_{i} |\phi_i(\vec{r})|^2 \delta(E - \epsilon_i) \tag{2.38}$$

where, $\phi_i(\vec{r})$ are the single electron wavefunctions. Thus, we sum over each state such that the contribution from each state is weighted by the density of that state at that point. In an inhomogeneous system like moiré structures, LDOS is a more useful quantity, since, $\rho(\vec{r}, E)$ contains more information than $\rho(E)$. In order to compute the LDOS, we implement,

$$\rho(\vec{r}, E) = \sum_{n,k} |\psi_{n,k}(\vec{r})|^2 \ \delta(E - \epsilon_n) \tag{2.39}$$

where $\psi_{n,k}$ is a bloch state which is the n^{th} eigenfunction obtained from the SCF convergence with crystal wave number k and the ϵ_i are the Kohn-Sham eigenvalues.

Since we do a periodic calculation with the edges of the moiré cell as the periodic boundary, the eigenfunctions are Bloch states and need to be summed over k. In this thesis, since we are studying a 2d material, we compute a further integral over z to obtain $\rho(x, y, E)$.

$$\rho(x, y, E) = \sum_{n,k} \int |\psi_{n,k}(\vec{r})|^2 dz \ \delta(E - \epsilon_n)$$

In order to numerically compute LDOS, we implement the formula with a finite spread approximation of the delta function,

$$\rho(x, y, E) = \sum_{n,k} \int |\psi_{n,k}(\vec{r})|^2 dz \; \frac{1}{\sigma\sqrt{2\pi}} \exp\left[-\frac{(E - \epsilon_n)^2}{2\sigma^2}\right] \tag{2.40}$$

In the above equation, since, $\psi_{n,k}(\vec{r})$ and ϵ_n are obtained from the Kohn-Sham equations, the value of ϵ_n does not correspond to the energy expectation of the wavefunction. Hence, the above equation is an approximation of the actual LDOS. We use this equation as implemented in CP2K [21]. The quantity $\rho(x, y, E)$ is computed for a wide range of E and for every point (x, y) in the discretized real space within the moiré cell and a 2×2 mesh in the k-space. However, attempting to analyze the LDOS (denoted as $\rho(x, y, E)$) at every single point within the moiré cell is impractical. This is because LDOS near an atomic nucleus is likely to be very different from one that is away from any atom.

This inherent small-scale variability poses a challenge, as it obscures the differences in LDOS due to variations in interlayer alignment across the moiré structure. To address this, we adopt a systematic approach. We divide the moiré cell's area into one hundred discrete bins in a 10×10 grid. The LDOS is then calculated at every point (x, y) in the discretized real space, and then, we average the LDOS within each bin.

$$\rho_{\text{avg}}(x_i, y_i, E) = \frac{1}{A} \iint_{S_i} \rho(x, y, E) d\sigma \tag{2.41}$$

where S_i is the i^{th} bin with area A which is one hundredth the area of the moiré cell.

Since this binned LDOS is averaged over a region with many atoms, we can use it to calculate the local valence and conduction band edges for that region.

2.10 Valence and Conduction Band Edges

In solid state physics, the electrons are in quantum states that are superpositions of a very large number of atomic orbitals. In the limit of very large systems, the energy spacing between the multi-atom orbitals become negligibly small. We can thus assume that the electron states form continuous

bands of energy levels. The band closest to the Fermi level and just below it is called the valence band while the one just above it is called the conduction band. The energy gap between the highest point of the valence band (the valence band edge) and the lowest point of the conduction band (the conduction band edge) is called the band gap.

In order to find the local band edges for our system from the LDOS, we use a specific cutoff LDOS, ρ_0. The energies for which the bin averaged LDOS is below this cutoff are disregarded for the calculation of the local valence and conduction band edges. The reason for this cutoff is that we expect a certain amount of spreading from quantum mechanics. This causes the states localized to one region to be found with a very low probability in another region. This leads to a small contribution to the LDOS in one region due to the states present in another region which introduces inaccuracies in the local band edge determination. By imposing this cutoff, we ensure that only electron states with significant contributions to the LDOS within a given region are considered for the determination of the local band edges.

Thus, the local valence band maximum (VBM) is the highest value of E below the Fermi level, for which the binned LDOS is higher than the cutoff, i.e.,

$$E^{\rho_0}_{\mathrm{VBM}}(x_i, y_i) = \max\{E | E < E_F \text{ and } \rho_{\mathrm{avg}}(x_i, y_i, E) > \rho_0\} \tag{2.42}$$

where, E_F is the Fermi energy given by,

$$E_F = \frac{1}{2}\left(\epsilon_{\mathrm{HOMO}} + \epsilon_{\mathrm{LUMO}}\right)$$

where ϵ_{HOMO} and ϵ_{LUMO} are the KS-DFT eigenvalues for the highest occupied molecular orbital and the lowest unoccupied molecular orbital respectively. Likewise, the local conduction band minimum (CBM) is the lowest value of E above the Fermi level, for which the binned LDOS is higher than the cutoff.

$$E^{\rho_0}_{\mathrm{CBM}}(x_i, y_i) = \min\{E | E > E_F \text{ and } \rho_{\mathrm{avg}}(x_i, y_i, E) > \rho_0\} \tag{2.43}$$

Once the VBM and CBM are determined for each of the bins, the local band gap can then be calculated as the difference between them, i.e.,

$$E^{\rho_0}_{\mathrm{GAP}} = E^{\rho_0}_{\mathrm{CBM}} - E^{\rho_0}_{\mathrm{VBM}} \tag{2.44}$$

In this thesis, all our DFT calculations are done using CP2K [21] with atomic

centred gaussian basis sets. We used the DZVP (Double Zeta Valence Polarization) basis set [section 2.7] for all geometry optimization calculations. We used the TZVP (Triple Zeta Valence Polarization) basis set [section 2.7] for LDOS calculations. For the calculations of LDOS, we divide the k-space into a 2×2 mesh and sum over each point. For the calculation of the local valence and conduction band edges, we used a cutoff of $\rho_0 = 1\text{eV}^{-1}\text{nm}^{-2}$

Chapter 3

Results-I: VBM And CBM

In this chapter and the next, we discuss the results obtained during the duration of the research conducted on the H-stacked TMD moiré structure made of $MoSe_2$ and WSe_2. We begin by presenting the results of the LDOS calculations conducted and the differences of the LDOS at different stacking regions of the moiré cell. We use the LDOS obtained to calculate the band edges and band gap for this system. We then describe the band edge surfaces obtained from this calculation. Finally, we show that the extent of the variation in the band edges, which is a measure of the moiré potential increases with the moiré length. We shall study the causes and parametric dependence of this variation in the following chapter.

3.1 Overview Of The System

As described in the first chapter, the system under study is the moiré structure made by overlaying $MoSe_2$ on WSe_2. In order to study this material, we prepare moiré cells with various angles (and thus moire lengths). The exact mathematics used to construct the moiré cell is described in the appendix section A.1. Each moiré cell is comprised of two layers of TMD layers, one of $MoSe_2$ and one of WSe_2. Since each TMD layer comprises of one layer of metal atoms (W or Mo) in between two layers of nonmetal atoms (Se), in effect, we have six layers of atoms of various types.

Each of the TMD layers is constructed using cell parameters that are DFT optimized for the TMD monolayer from the Computational 2D Materials Database (C2DB) [22] [23]. Each of six atomic layers are completely flat since the atoms each have the same Z component of position. It is known from spectroscopy experiments that the moiré structure prepared from these

TMDs have a non-trivial height variation [1]. Thus, we expect the atoms to move around in the lattice when the system is prepared.

In order to find the positions of atoms in these systems, we perform a geometry optimization calculation for the moiré cell using DFT with the PBE functional and gaussian DZVP basis [24]. During the geometry optimization, we do not optimize the cell length of the moiré cell since the unoptimized structures are made using the DFT optimized lattice parameters for each of the TMD layers. Using the geometry optimized moiré cell, we perform a DFT calculation to obtain the ground state density function using the PBE functional and TZVP. We use this to find the local density of states as described in section 2.9.

We present the results of the LDOS calculations and interpret them and discuss the causes of the band edge variations obtained.

3.2 Local Density of States

As described in 2.9, we divide the moiré cell into a hundred regions called bins. We then calculate the LDOS for every point in the moiré cell, integrate over the z-axis and average over each of the bins as described in equation (2.41). The bin averaged LDOS plots for two regions within a moiré cell are shown in figure 3.1.

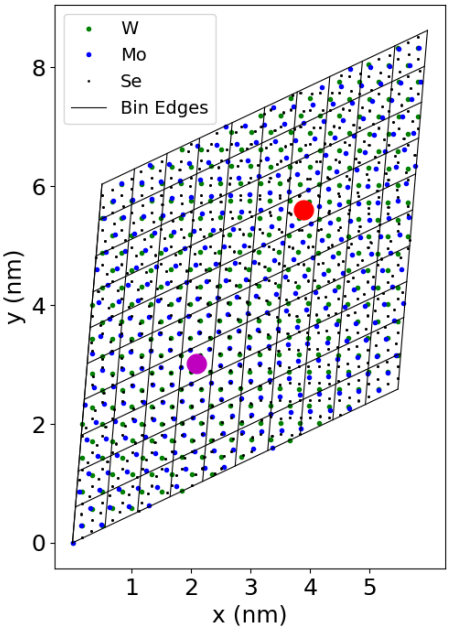

(a) A TMD moiré cell with 2010 atoms. The LDOS for the bins highlighted in red and magenta are shown.

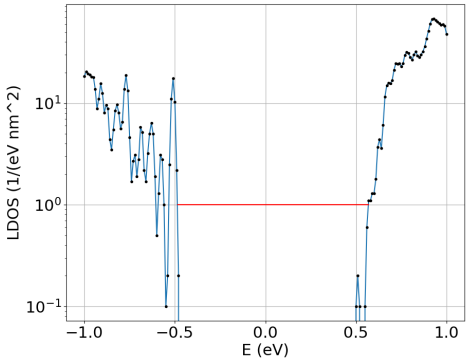

(b) $\rho_{\text{avg}}(x_i, y_i, E)$ at the magenta spot

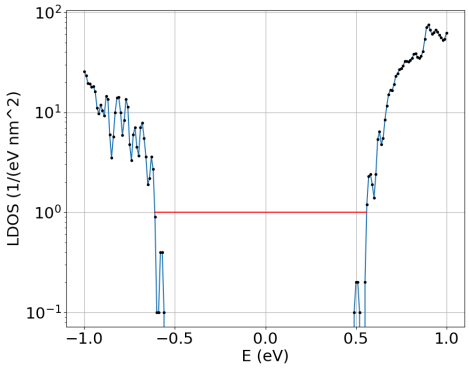

(c) $\rho_{\text{avg}}(x_i, y_i, E)$ at the red spot

Figure 3.1: **LDOS plots at two different regions of the moiré cell**
Figure (a) shows the structure of the moiré cell with 2010 atoms divided into 100 bins. The LDOS is calculated at every point in the cell, integrated over the z-axis and averaged over each bin.
This bin-averaged LDOS is shown for two bins highlighted in magenta and red in figure (b) and (c). The magenta spot is in the H_X^M region while the red spot is in the H_X^X region. The energy scale in (b) and (c) is set to zero at the Fermi level.
The red line in (b) and (c) is the cutoff LDOS at $1\text{eV}^{-1}\text{nm}^{-2}$. The points where the ends of the line meet the LDOS plots are the valence and conduction band edges and the length of the red line is the band gap.

As explained in section 1.2, each H-stacked moiré cell has three stacking regions called H_M^M, H_X^M and H_X^X regions. As depicted in figure 3.1, our analysis shows us that there is notable disparity in the local density of states across various regions within the moiré cell. The local VBM is 3.40 eV on the red

sport, and 3.28 eV on the magenta spot. This is a difference of about 120 meV which is called the moiré potential. The CBMs are 4.46 eV and 4.44 eV on the red and magenta spots respectively with a difference of 20meV which is not very high. The band gaps are 1.05 eV and 1.17 eV on the red and magenta spots respectively with a band gap difference of about 120 meV. These values show quite clearly that the band edges vary quite significantly in the different regions of the moiré cell.

In the following section, we shall further examine the spatial variability of the band edges.

3.3 Local Band Edge Variation

We utilize the band edges derived from each of the 100 bins (section 2.9) using equations (2.42) and (2.43) and use cubic interpolation to extrapolate these edges across the entire moiré cell. Similarly, we can construct band gap surfaces using the band gap values calculated using equation (2.44).

Since we know the average LDOS for every bin, we can assign this value at the center of the bin. We then use cubic interpolation to estimate the bin averaged VBM, CBM and band gap at other points. That is, we estimate what they would have been if we calculated their values by using a bin averaged LDOS with a bin centered at that point. This process enables us to construct band edge surfaces for both the conduction and valence bands. The band edge surfaces thus obtained are shown in figure 3.2.

Figures 3.2a and 3.2b show us the spatial distribution of both the conduction and valence band edges within the moiré structure. Notably, these band edges exhibit spatial variation across the surface. Furthermore, discernible small domains emerge where the band edge values remain relatively constant. This spatial heterogeneity arises from the variation of local atomic arrangements and electronic properties within the moiré cell.

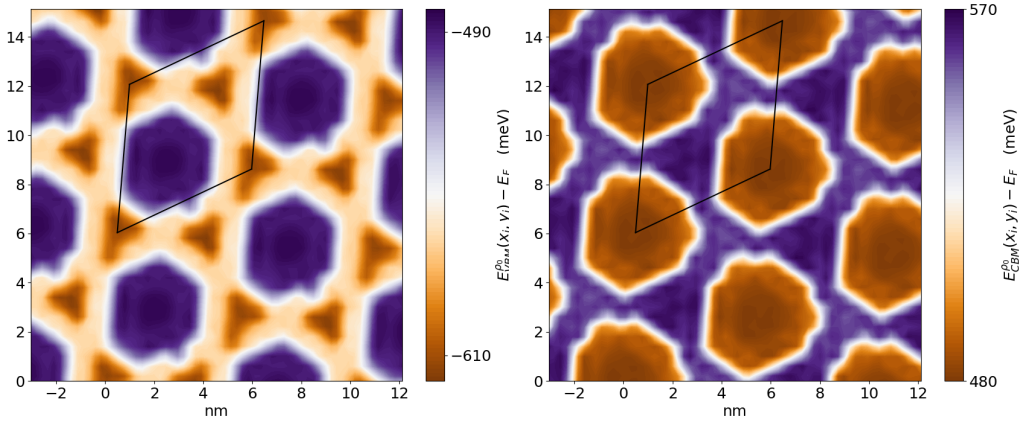

(a) Valence Band Edge Map (b) Conduction Band Edge Map

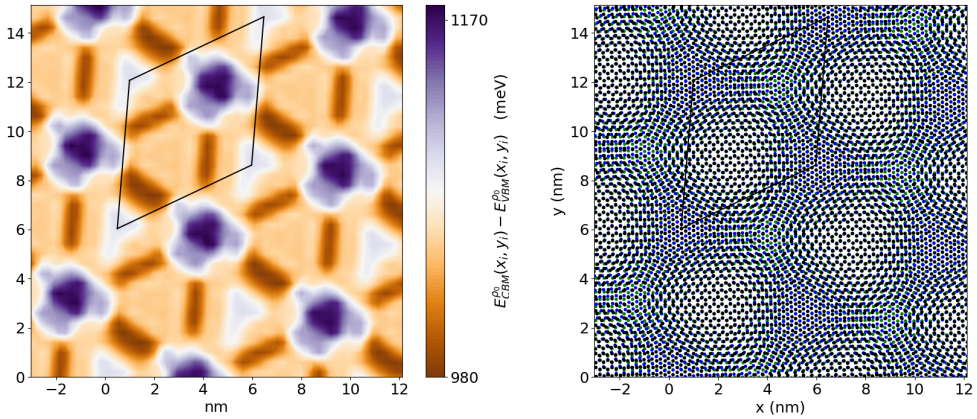

(c) Local Band Gap Map (d) Moiré structure for comparison

Figure 3.2: Local band edge and local band gap maps for TMD moiré cell with 2010 atoms, $\rho_0 = 1\text{eV}^{-1}\text{nm}^{-2}$

We now present the band edge results for another moiré cell with 1839 atoms and a twist angle of 3.2°.

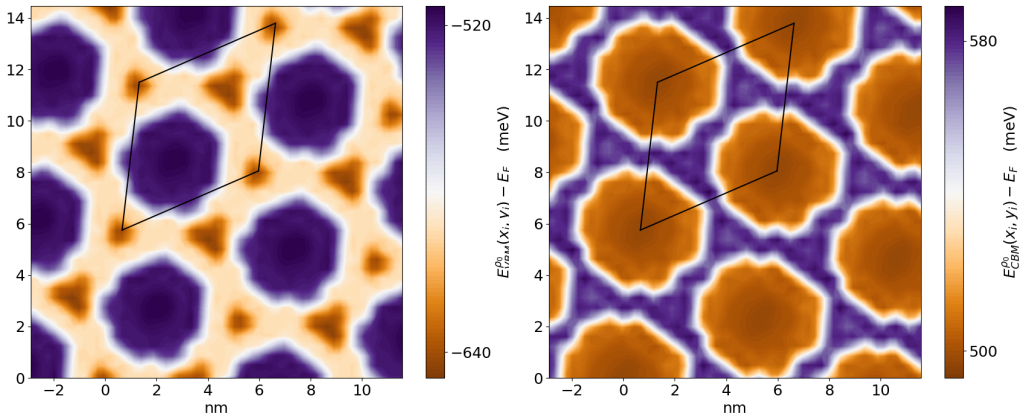

(a) Valence Band Edge Map (b) Conduction Band Edge Map

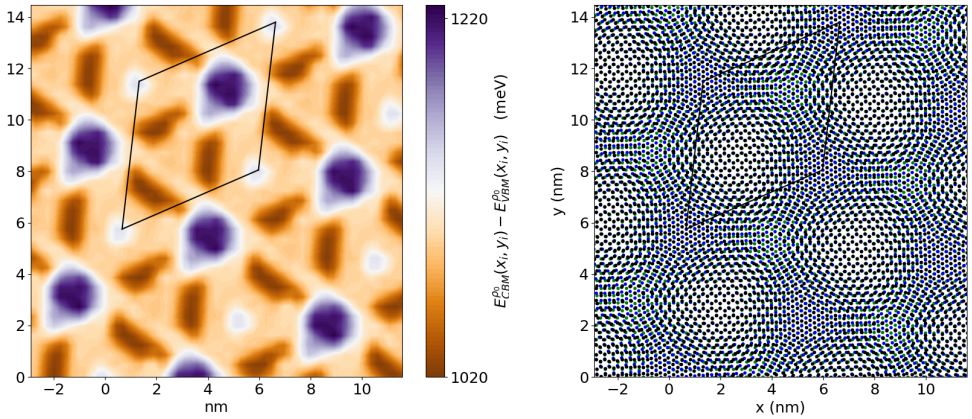

(c) Local Band Gap Map (d) Moiré structure for comparison

Figure 3.3: Local band edge and local band gap maps for TMD moiré cell with 1839 atoms, $\rho_0 = 1\text{eV}^{-1}\text{nm}^{-2}$

We see that qualitatively, the valence band and conduction band edges and the local band gap form a similar pattern for a different moiré length. Quantitatively, we see that the extent to which the local band edges vary are quite different.

The patterns we observed in our band edge calculations look quite similar to the ones observed in the experiments as shown in 3.4.

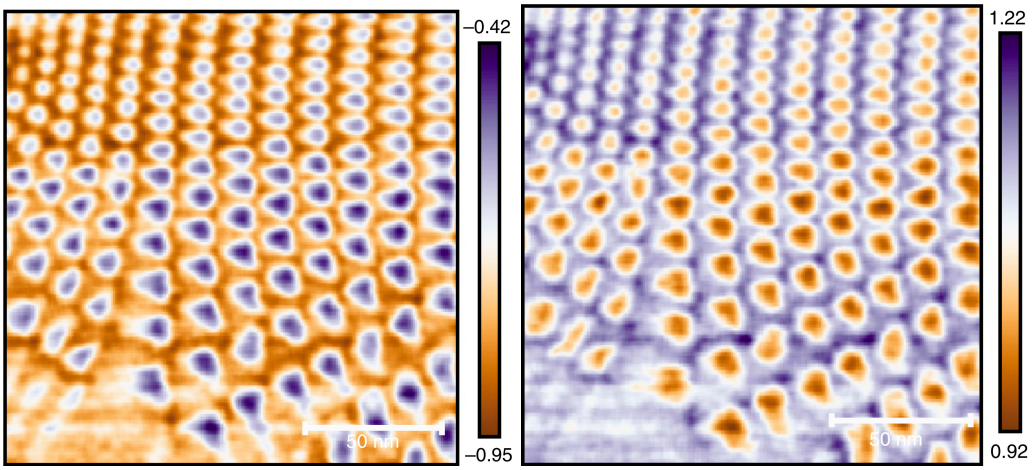

(a) Valence band edge (b) Conduction band edge

Figure 3.4: Experimentally determined band edge maps (taken from [1])

One significant difference is that the valence band edge maximum and the conduction band edge minimum occur in the same region in the experiment while in our calculations, we see that they occur in different places (with a shift). Another difference is that in the experiment, the moiré wavelength is not consistent across cells. The moiré wavelength interpolates continuously between a minimum of 5 nm to greater than 20 nm while our study is limited to moiré cells with wavelength only up to 6 nm.

3.4 Dependence on moiré length

We repeated the calculations of the LDOS and band edges for several systems by varying the twist angle to get moiré cells of varying moiré lengths. We found that the extent of the variation in the local valence edge, conduction edge and the bandgap depended on the moiré length as shown in 3.5.

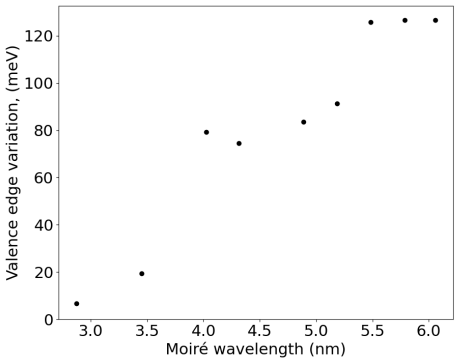

(a) Spatial variation of the VBM

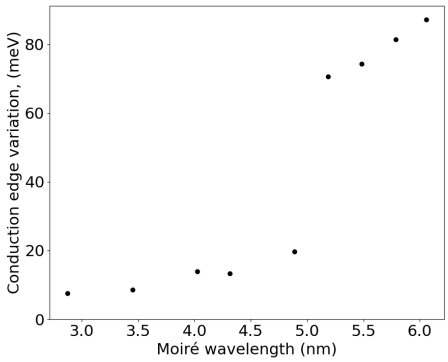

(b) Spatial variation of the CBM

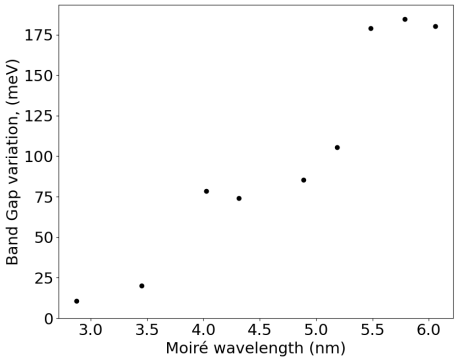

(c) Spatial variation of the band gap

Figure 3.5: Variability of the band gap and band edges as a function of the moiré length

Our finding is that, the larger the moiré length, the larger is the extent of the moiré potential. In the experiment presented in [1], they found that the moiré potential increases with the moiré wavelength and reaches a maximum at around 12 nm as shown in figure 3.6. Thus, our result is in agreement with the experimental data (although, in the experiment they have not studied this for the structures with moiré wavelength smaller than 6 nm which is the moiré wavelength of our largest structure).

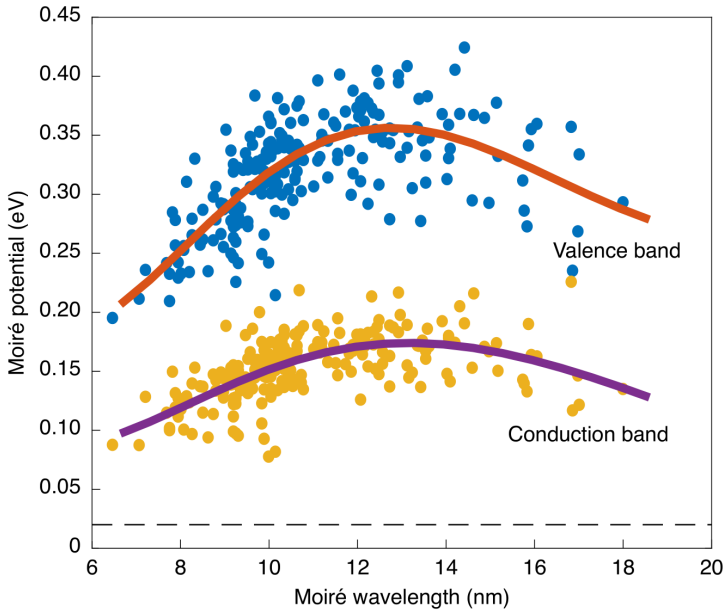

Figure 3.6: **Moiré potential as a function of moiré wavelength** extracted from spectroscopic imaging experiments. Solid lines are fifth-order fits to the data. Taken from [1]

3.5 Discussion

This section provides a summary and discussion of the results presented in this chapter.
We saw in section 3.2 that the moiré structures we constructed and geometry optimized did not have the same LDOS at different regions of the moiré cell. We computed the conduction and valence band edges using the LDOS and obtained band edge maps for the system. We saw that different regions of the moiré cell with varying interlayer alignments had different local band edges.

The variation in the low energy electronic structure can be modelled as the consequence of a spatially varying potential imposed on a single layer. This spatially varying potential is called the moiré cell. The extent of the variation of the band edges is thus a measure of the strength of the moiré potential.

In order to study the moiré potential, we used the band edges obtained to construct a band edge map using cubic interpolation. The band edge map thus obtained has several interesting features. The valence band edge map showed us that the moiré cell had large patches with a very high valence

band edge and small triangular regions with a low valence band edge. The conduction band edge on the other hand had patches with a very low band edge and small regions with very high conduction band edge. We also see that the regions with the large patches in the valence and conduction band are distinct. This means that the region with the conduction band minimum does not coincide with the region of valence band maximum.
Comparing with the structure shown in figure 3.2d we see that the three alignment types described in section 1.2 have three different regimes for conduction and valence band edges.

The band edge minima and maxima occur as follows:

1. The H_M^M region (on the corners of the inscribed rhombus) is the valence band minimum and the conduction band minimum.

2. The H_X^M region (also called the H_X^M region) which is visibly the lightest in the structure as seen in figure 3.2d has the valence band maximum and the conduction band minimum.

3. The H_X^X region has one of the valence band minima and a a moderately high value of conduction band. This region is lighter blue in the conduction band edge map in figure 3.2b and brown in the valence band edge map in 3.2a. This region has the highest band gap.

Notice that the lowest band gap does not occur in any of the regions listed but in between the H_M^M and H_X^M regions. The rectangular regions that separate the H_M^M and H_X^M regions are domain walls of transition stacking usually called solitons or strain solitons.

We performed this analysis for 10 structures with various lengths and angles and found that the strength of the moiré potential increases with increasing moiré length as shown in figure 3.5 which was in agreement with the experiment in [1] (figure 3.6).
In the following chapter, we shall probe the causes for the large spatial variability in the band edges and the reason for the increase in the moiré potential with increasing moiré length.

Chapter 4

Results-II: Altering The Structures

So far, we have seen that the valence and conduction band edges vary greatly in space. We have also seen that the extent of variability, which indicates the strength of the moiré potential, increases with the moiré length. The moiré potential could be due to the internal strain in the TMD layers or it could be due to differences in the interlayer coupling. We shall now probe the reason and parametric dependence of this variability. The way we do this is by altering the structure of the moiré pattern and examining the variation in the conduction and valence band edges. In this chapter, we shall summarize and discuss the results obtained by performing our analysis on altered structures.

4.1 Band Edge Variations For The Structures Without Geometry Optimization

In this section, we present the results for the calculations of the band edges obtained from LDOS calculations for the structures without geometry optimization. For such structures, there is no in-plane strain and there is a constant inter-layer gap. The two TMD layers have the same structure as they would have in the absence of the other layer since they each layer simply assumes the structure of the TMD monolayer.

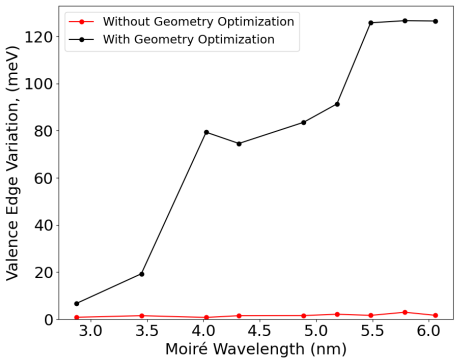

(a) Valence band edge variation

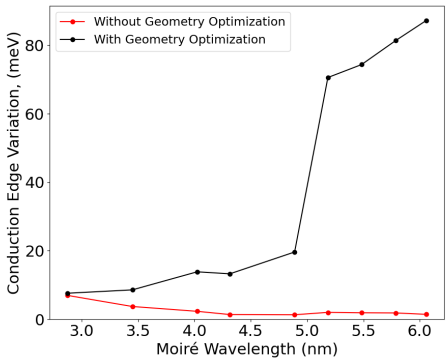

(b) Conduction band edge variation

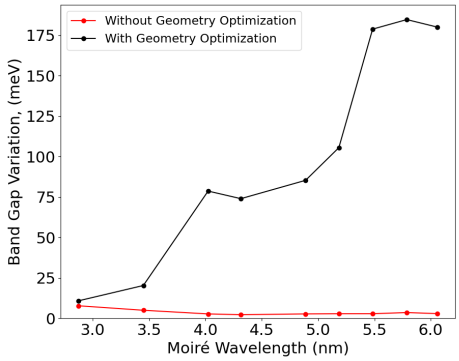

(c) Band Gap variation

Figure 4.1: **Band edge and band gap variations for the cases with and without geometry optimization** Figure (a) and (b) compare the extent of the variation in the valence band edge and the conduction band edge with and without geometry optimization. Figure (c) compares the extent of the band gap variation in the two cases.

As we can see in figure 4.1, the extent of the band edge variation and the band gap variation is negligibly small and non-increasing for the structures without geometry optimization compared to the geometry optimized structures.

We thus conclude that the geometry optimization changes the structures in a way that increases the variation in the band edges. We hypothesize that the extent of the change from geometry optimization is also dependent on the moiré length and thus, larger the moiré length, greater is the geometry alteration and thus greater is the extent of the variation.
One of the changes that the geometry optimization causes is the variation in

the interlayer gap as shown in figure 4.2.

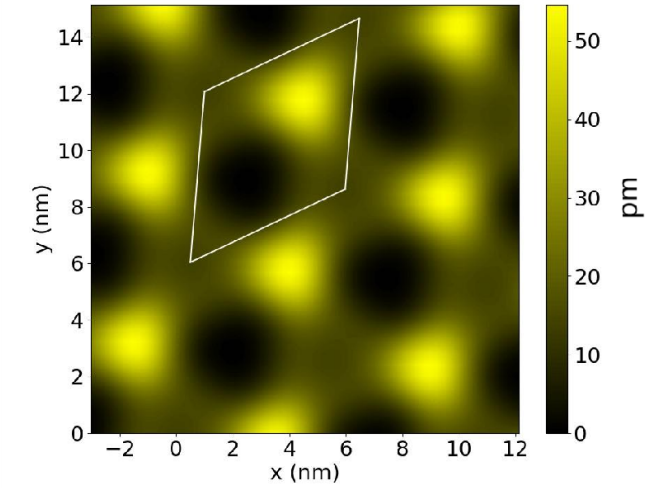

Figure 4.2: **Variability of the interlayer separation** for a moiré structure with 2010 atoms

Let us now examine the extent of the interlayer gap variation in the geometry optimized structures as a function of the moiré length for the 10 different moiré cells with different values of moiré length as shown in figure 4.3.

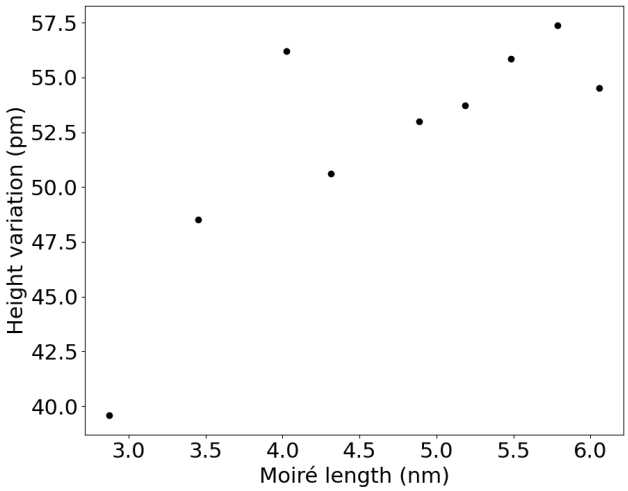

Figure 4.3: Variability of the interlayer separation as a function of moiré length

We find that the extent of the interlayer gap variation increases with increasing moiré length. We can thus hypothesize that the variation in the interlayer gaps is the cause of the band edge variation.

In order to test our hypothesis, we perform the LDOS and band edge calculations for the structures after altering them to eliminate height variations as described in the following section.

4.2 Flattened Geometry

In order to test our hypothesis, we alter the geometry optimized moiré cell as follows:

1. We divide the cell vertically into the 6 atomic layers, 4 of non-metals and 2 of metals.
2. We then average over the Z position of all the atoms for each of the layers.
3. Finally, we replace the Z position of each of the atoms with the average Z position for that layer, effectively flattening each layer.

We use this altered geometry to compute the ground state electron density and calculate the LDOS. We measure the band edges and the band edge variation for each of the systems. The band edges for this altered system and the original geometry optimized system are plotted in figure 4.4.

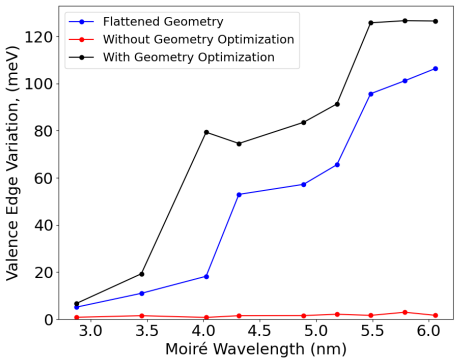

(a) Valence band edge variation

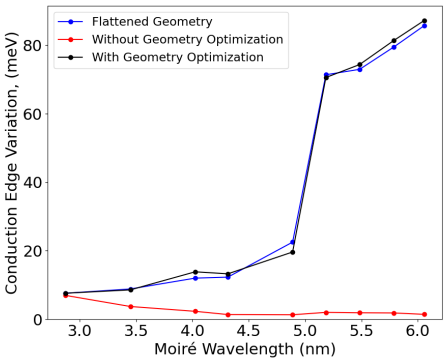

(b) Conduction band edge variation

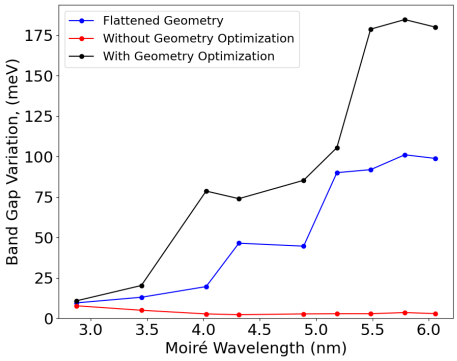

(c) Band Gap variation

Figure 4.4: A comparison of the band edge and band gap variations for the cases without geometry optimization and with and without interlayer gap variation

We see in figure 4.4 that the flattened geometry has a significantly different valence edge variation and thus a different band gap variation. However, we see that the effect of the flattening on the conduction band edge is minimal.

4.3 In-Plane Frozen Geometry

The other way in which we can alter the geometry optimized cell is by freezing the motion of the atoms in-plane while allowing motion in the Z direction. We do this by replacing the X and Y values of the atomic position of each of the atoms with the X and Y values of the geometry optimized unit cell. The band edge variation for these altered systems are plotted in figure 4.5.

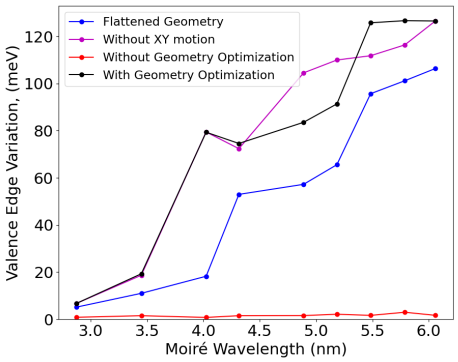

(a) Valence band edge variation

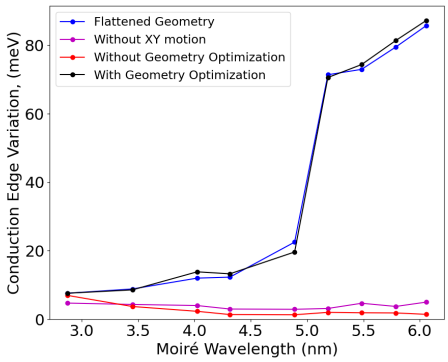

(b) Conduction band edge variation

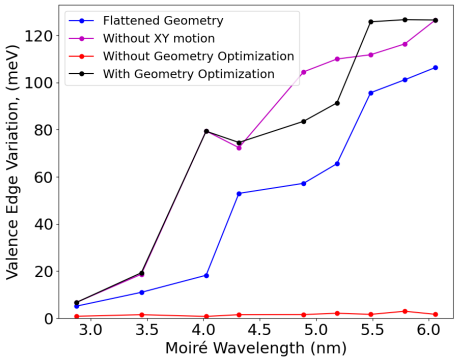

(c) Band gap variation

Figure 4.5: A comparison of the band edge and band gap variations for all the four cases

We see that in the case of the valence edge variation, all three systems show similar values for all structures. However, for the conduction edge variation, the effect of freezing in-plane motion is very significant.

4.4 Discussion

In this chapter, we saw that the band edge variations observed in our TMD moiré structure were significantly smaller for the structures if no geometry optimization was performed. We therefore learnt that the alteration in the geometry in each layer due to the presence of the other layer is a major

contributor to the moiré potential. In order to further understand the exact nature of the moiré potential's dependence on the geometry, we altered the structures by freezing the atomic in-plane motion while allowing height variations in one case and by flattening the structure while allowing in-plane motion in another case.

By doing so, we were able to find out whether the internal strain, or the interlayer coupling are the dominant factors in determining the spatial conduction edge variation and valence edge variation for each of the moiré cells. We see that the conduction edge variation has been very nearly zero for all the structures with frozen in-plane motion while flattening the structure had no effect on the conduction edge variation. We thus conclude that the in-plane strain is significantly more important in determining the moiré potential for the conduction band than the interlayer coupling.

On the other hand, in the case of the valence edge, however, we see that the effect of freezing in-plane motion led to a small change in the effect of the moiré potential while flattening the geometry reduced the effect of the moiré potential significantly as seen in figure 4.5a. We therefore conclude that in-plane strain and interlayer coupling affect the spatial variation of the conduction and valence band edges differently and to a different extent.

No experimental data exists for the computational results presented in this chapter as it requires precise control of the positions of all the atoms and such alterations to the TMD moiré structures have not been performed.

Chapter 5

Conclusion And Future Direction

In this thesis, we studied transition metal dichalcogenide moiré structures made by overlaying $MoSe_2$ on WSe_2. Each of the structures was studied by constructing the moiré cell and using geometry optimization to obtain the optimal structures and performing density functional theory calculations to get the local density of states (LDOS). We used the LDOS obtain the local conduction band maxima and valence band minima at various locations in the moiré cell. We found that there is significant difference in the band edges at different locations of the cell. Using the local band edges we obtained the band edge maps which showed that the band edge variation is of the order of 100 meV.

When we repeated this procedure for 10 different moiré cells, each with a different moiré length, we saw that the extent to which the band edges vary in space, which is a measure of the moiré potential, increases with the moiré length. Therefore, we see that the moiré potential is much stronger for structures with a larger moiré length.

In order to probe the structural causes for the moiré potential, we calculated the LDOS and local band edges for the moiré cells without first doing geometry optimization. When we did this, we saw that the extent of band edge variation decreased significantly to an order of 10 meV. We therefore conclude that geometry optimization changes the structures in a way that greatly increases the moiré potential.

We can divide the motion of the atoms during geometry optimization into two components: out of plane motion (in the z direction) and in-plane motion (in the xy plane). In-plane motion changes the in-plane strain in the

lattice and out of plane motion changes the interlayer coupling.

In order to probe which of these two structural effects more significantly affect the conduction and valence band edges, we altered the geometry optimized structures and obtained the LDOS for these altered structures. We altered the structures in two ways. In the first case, we flattened the structure by replacing the z value of every atom by the average z value of that atomic layer. In the second case, we froze in-plane motion by replacing the x and y value of the position of every atom by the x and y value of the position of the unoptimized structures.

When we performed LDOS calculations, in the case of the flattened structures, we saw nearly no change to the extent of the variation in the conduction band edge while the extent of valence band edge variation decreased significantly. In case of the frozen in-plane motion, we saw that the conduction edge variation became as small as the case with no geometry optimization while the valence band edge variation was not significantly affected (especially for the smaller structures).

We thus conclude that spatial variation in the in-plane strain and not the interlayer coupling is the most important structural contributor to the conduction band edge. For the valence band edge, the variation in the interlayer coupling contributes to the band edge variation significantly more than the in-plane strain.

In this thesis we found that for the geometry optimized structures, the variation in the band edges, which is a measure of the moiré potential, is of the order of 100 meV, while for the same structures without geometry optimization, we obtain a moiré potential of the order of 10 meV.

Experimental observations reveal the moiré potential to be of the order of 100 meV [1]. Moiré potentials of such a large magnitude are referred to as 'deep moiré potentials' [1]. Previous studies that do not include lattice relaxation effects (such as [25]) calculate a 'shallow' moiré potential of the order of 10 meV.

It is known from experiments that moiré structures undergo a significant amount of atomic relaxation [26]. In this thesis, we have compared the moiré potential for the same structures with and without geometry optimization and confirmed that atomic relaxation significantly increases the moiré poten-

tial. We have thus confirmed recent theoretical works like [3] and [4] which calculate 'deep' moiré potentials of the order of 100 meV.

We also obtained band edge maps from the LDOS computations and found that the extent of variation and shapes of the regions of high valence band maximum and low conduction band minimum were similar to the ones observed in [1]. One major discrepancy observed between our calculations and the experimental data (from [1]) is that, in our work, we saw that the regions of low conduction band minimum and the regions of high valence edge maximum do not occur at the same region, unlike in the experiments (figure 3.4) where they are overlapping.

Finally, our study also agreed with the experiment that the strength of the moiré potential increases with increasing moiré wavelength. However, in the experiment, the smallest moiré cells had a wavelength of 6nm which is the length of the largest cell we studied. This points to a need for computational methods and tools that enable dft calculations for structures with several thousand atoms in the unit cells.

From the work presented in this thesis, we can conclude that the technique established in this investigation is applicable for computing the moiré potentials in transition metal dichalcogenide bilayers. Moreover, we can employ this approach to address particular inquiries regarding the parametric influence of the moiré structure on the moiré potential which is either extremely difficult or impossible to do in experiments.

This method can be used to better examine the moiré potential and the behaviour of excitons for future work. In the structures that we studied, we found that the valence band maximum and the conduction band minimum are located at different regions of the moiré cell. This can lead to excitons with the electron and the hole spatially segregated in the moiré cell as described in [13] which must be further studied in the future.

References

[1] Sara Shabani, Dorri Halbertal, Wenjing Wu, Mingxing Chen, Song Liu, James Hone, Wang Yao, Dmitri N Basov, Xiaoyang Zhu, and Abhay N Pasupathy. Deep moiré potentials in twisted transition metal dichalcogenide bilayers. *Nature Physics*, 17(6):720–725, 2021.

[2] Fengcheng Wu, Timothy Lovorn, Emanuel Tutuc, and Allan H MacDonald. Hubbard model physics in transition metal dichalcogenide moiré bands. *Physical review letters*, 121(2):026402, 2018.

[3] WT Geng, V Wang, YC Liu, T Ohno, and J Nara. Moiré potential, lattice corrugation, and band gap spatial variation in a twist-free $MoTe_2/MoS_2$ heterobilayer. *The Journal of Physical Chemistry Letters*, 11(7):2637–2646, 2020.

[4] Gautam Jha, Wei Li, Thomas Brumme, and Thomas Heine. Spin orbit coupling effects on the excitonic properties of twisted moiré transition metal dichalcogenides. *Preprint, ChemRxiv*, 2023.

[5] K. S. Novoselov, A. K. Geim, S. V. Morozov, D. Jiang, Y. Zhang, S. V. Dubonos, I. V. Grigorieva, and A. A. Firsov. Electric field effect in atomically thin carbon films. *Science*, 306(5696):666–669, 2004.

[6] C Dean, Lei Wang, P Maher, Carlos Forsythe, Fereshte Ghahari, Y Gao, Jyoti Katoch, Masa Ishigami, Pilkyung Moon, Mikito Koshino, Takashi Taniguchi, K Watanabe, K Shepard, James Hone, and Phaly Kim. Hofstadter's butterfly and the fractal quantum hall effect in moire superlattices. *Nature*, 497:598, 05 2013.

[7] Lei Wang, En-Min Shih, Augusto Ghiotto, Lede Xian, Daniel A Rhodes, Cheng Tan, Martin Claassen, Dante M Kennes, Yusong Bai, Bumho Kim, et al. Correlated electronic phases in twisted bilayer transition metal dichalcogenides. *Nature materials*, 19(8):861–866, 2020.

[8] Emma C Regan, Danqing Wang, Chenhao Jin, M Iqbal Bakti Utama, Beini Gao, Xin Wei, Sihan Zhao, Wenyu Zhao, Zuocheng Zhang, Kentaro Yumigeta, et al. Mott and generalized wigner crystal states in WSe_2/WS_2 moiré superlattices. *Nature*, 579(7799):359–363, 2020.

[9] Kin Fai Mak, Changgu Lee, James Hone, Jie Shan, and Tony F. Heinz. Atomically thin MoS_2: A new direct-gap semiconductor. *Phys. Rev. Lett.*, 105:136805, Sep 2010.

[10] Thomas Mueller and Ermin Malic. Exciton physics and device application of two-dimensional transition metal dichalcogenide semiconductors. *npj 2D Materials and Applications*, 2(1):29, 2018.

[11] Kyle L Seyler, Pasqual Rivera, Hongyi Yu, Nathan P Wilson, Essance L Ray, David G Mandrus, Jiaqiang Yan, Wang Yao, and Xiaodong Xu. Signatures of moiré-trapped valley excitons in $MoSe_2/WSe_2$ heterobilayers. *Nature*, 567(7746):66–70, 2019.

[12] A de la Torre, DM Kennes, E Malic, and S Kar. Spatial inhomogeneities, moiré potential and moiré excitons. *arXiv preprint arXiv:2402.19236*, 2024.

[13] Mit H Naik, Emma C Regan, Zuocheng Zhang, Yang-Hao Chan, Zhenglu Li, Danqing Wang, Yoseob Yoon, Chin Shen Ong, Wenyu Zhao, Sihan Zhao, et al. Intralayer charge-transfer moiré excitons in van der waals superlattices. *Nature*, 609(7925):52–57, 2022.

[14] Pierre Hohenberg and Walter Kohn. Inhomogeneous electron gas. *Physical review*, 136(3B):B864, 1964.

[15] W. Kohn and L. J. Sham. Self-consistent equations including exchange and correlation effects. *Phys. Rev.*, 140:A1133–A1138, Nov 1965.

[16] Robert G. Parr and Yang Weitao. *Density-Functional Theory of Atoms and Molecules*. Oxford University Press, USA, 1994.

[17] Richard M. Martin. *Electronic Structure: Basic Theory and Practical Methods*. Cambridge University Press, 2004.

[18] F. Jensen. *Introduction to Computational Chemistry*. Wiley, 2013.

[19] H. Hellmann. *Einführung in die quantenchemie*. F. Deuticke, 1937.

[20] R. P. Feynman. Forces in molecules. *Phys. Rev.*, 56:340–343, Aug 1939.

[21] Thomas D Kühne, Marcella Iannuzzi, Mauro Del Ben, Vladimir V Rybkin, Patrick Seewald, Frederick Stein, Teodoro Laino, Rustam Z Khaliullin, Ole Schütt, Florian Schiffmann, et al. Cp2k: An electronic structure and molecular dynamics software package-quickstep: Efficient and accurate electronic structure calculations. *The Journal of Chemical Physics*, 152(19), 2020.

[22] Sten Haastrup, Mikkel Strange, Mohnish Pandey, Thorsten Deilmann, Per S Schmidt, Nicki F Hinsche, Morten N Gjerding, Daniele Torelli, Peter M Larsen, Anders C Riis-Jensen, et al. The computational 2d materials database: high-throughput modeling and discovery of atomically thin crystals. *2D Materials*, 5(4):042002, 2018.

[23] Morten Niklas Gjerding, Alireza Taghizadeh, Asbjørn Rasmussen, Sajid Ali, Fabian Bertoldo, Thorsten Deilmann, Nikolaj Rørbæk Knøsgaard, Mads Kruse, Ask Hjorth Larsen, Simone Manti, et al. Recent progress of the computational 2d materials database (c2db). *2D Materials*, 8(4):044002, 2021.

[24] Sandro Chiodo, Nino Russo, and Emilia Sicilia. Newly developed basis sets for density functional calculations. *Journal of Computational Chemistry*, 26:175–183, 01 2005.

[25] David A Ruiz-Tijerina and Vladimir I Fal'ko. Interlayer hybridization and moiré superlattice minibands for electrons and excitons in heterobilayers of transition-metal dichalcogenides. *Physical Review B*, 99(12):125424, 2019.

[26] Astrid Weston, Yichao Zou, Vladimir Enaldiev, Alex Summerfield, Nicholas Clark, Viktor Zólyomi, Abigail Graham, Celal Yelgel, Samuel Magorrian, Mingwei Zhou, et al. Atomic reconstruction in twisted bilayers of transition metal dichalcogenides. *Nature nanotechnology*, 15(7):592–597, 2020.

Appendix A

Additional data

A.1 Mathematics of Moiré Patterns

In order for two lattices to form a moiré pattern, we need the two lattices to form a larger pattern with agreement between the lattices at regular intervals. The moiré pattern effectively forms a much larger unit cell for the combined two-layer system called the "moiré cell".
To form a moiré pattern, a linear combination of the lattice vectors of one layer needs to be equal to a linear combination of the lattice vectors of another layer.
Let $\vec{a}_1$ and $\vec{a}_2$ be lattice vectors of the lower (WSe_2) lattice and let $\vec{b}_1$ and $\vec{b}_2$ be the lattice vectors of the upper ($MoSe_2$) lattice.

The required condition can then be expressed as:

$$n_1\vec{a}_1 + n_2\vec{a}_2 = m_1\vec{b}_1 + m_2\vec{b}_2 \tag{A.1}$$

where, n_1, n_2, m_1, and m_2 are integers.
Let l_a and l_b be the lattice constants of WSe_2 and $MoSe_2$ monolayers without strain.
Let $r = l_b/l_a$ be the ratio between the two lattice constants.
If l'_b is the lattice constant of the $MoSe_2$ layer with strain, define $s = l'_b/l_b$.
Let $R(\theta)$ be the active rotation operator in two dimensions where θ is the twist angle of this moiré pattern.
Therefore, we can express $\vec{b}_1$ and $\vec{b}_2$ in terms of $\vec{a}_1$ and $\vec{a}_2$ as follows:

$$\vec{b}_1 = rsR(\theta)\vec{a}_1$$
$$\vec{b}_2 = rsR(\theta)\vec{a}_2$$

And since for a honeycomb lattice, the angle between the two lattice vectors is $\pi/3$,

$$\vec{a}_2 = R\left(\frac{\pi}{3}\right)\vec{a}_1$$

Therefore, we can express $\vec{a}_2$, $\vec{b}_1$ and $\vec{b}_2$ in terms of $\vec{a}_1$.

$$\begin{aligned}
\vec{a}_2 &= R\left(\frac{\pi}{3}\right)\vec{a}_1 \\
\vec{b}_1 &= rsR\left(\theta\right)\vec{a}_1 \\
\vec{b}_2 &= rsR\left(\theta + \frac{\pi}{3}\right)\vec{a}_1
\end{aligned}$$

Equation (A.1) may be written as:

$$\begin{aligned}
n_1\vec{a}_1 + n_2R\left(\frac{\pi}{3}\right)\vec{a}_1 =& rsm_1R\left(\theta\right)\vec{a}_1 \\
&+ rsm_2R\left(\theta + \frac{\pi}{3}\right)\vec{a}_1
\end{aligned}$$

Therefore,

$$n_1 + n_2R\left(\frac{\pi}{3}\right) = rsm_1R\left(\theta\right) + rsm_2R\left(\theta + \frac{\pi}{3}\right)$$

This is a matrix equation. Equating the entries gives us:

$$\begin{aligned}
n_1 + n_2R\cos\left(\frac{\pi}{3}\right) &= rsm_1\cos\left(\theta\right) + rsm_2\cos\left(\theta + \frac{\pi}{3}\right) \\
n_2R\sin\left(\frac{\pi}{3}\right) &= rsm_1\sin\left(\theta\right) + rsm_2\sin\left(\theta + \frac{\pi}{3}\right)
\end{aligned}$$

The above equations can be solved to find rs and θ in terms of n_1, n_2, m_1 and m_2.
We find:

$$rs = \frac{\sqrt{n_1^2 + n_1n_2 + n_2^2}}{\sqrt{m_1^2 + m_1m_2 + m_2^2}}$$

and,

$$\theta = \tan^{-1}\left(\frac{\sqrt{3}n_2/2}{n_1 + n_2/2}\right) - \tan^{-1}\left(\frac{\sqrt{3}m_2/2}{m_1 + m_2/2}\right)$$

Expressing $\vec{b}_1$ and $\vec{b}_2$ as a linear combination of $\vec{a}_1$ and $\vec{a}_2$,

$$\vec{b}_1 = rs\left(\cos\theta - \frac{1}{\sqrt{3}}\sin\theta\right)\vec{a}_1 + rs\left(\frac{2}{\sqrt{3}}\sin\theta\right)\vec{a}_2$$
$$\vec{b}_2 = rs\left(-\frac{2}{\sqrt{3}}\sin\theta\right)\vec{a}_1 + rs\left(\cos\theta + \frac{1}{\sqrt{3}}\sin\theta\right)\vec{a}_2$$

Or,

$$\vec{b}_1 = \frac{2rs}{\sqrt{3}}\left[\sin\left(\theta + \frac{2\pi}{3}\right)\vec{a}_1 + \sin\left(\theta + \pi\right)\vec{a}_2\right]$$
$$\vec{b}_2 = \frac{2rs}{\sqrt{3}}\left[\sin\left(\theta + \pi\right)\vec{a}_1 + \sin\left(\theta + \frac{\pi}{3}\right)\vec{a}_2\right]$$

Since we are looking for moiré structures with large patches where atoms have similar alignment, we need $rs \approx 1$ and small values of θ.
Now, we can choose various values of n_1, n_2, m_1 and m_2 that give us appropriate values of s and θ and the moiré length. Once we know that the strain and theta values are acceptable, we can then use $\vec{a_2}$, $\vec{b_1}$ and $\vec{b_2}$ expressed in terms of $\vec{a_1}$ to construct the moiré supercell.